JOURNAL OF GEOPHYSICAL RESEARCH, VOL. 102, NO. D10, PAGES 11,201–11,218, MAY 27, 1997

Retrieval of land surface parameters from airborne POLDER bidirectional reflectance distribution function during HAPEX-Sahel

Jean-Louis Roujean,[1] Didier Tanré,[2] François-Marie Bréon,[3] and Jean-Luc Deuzé[2]

Abstract. Spaceborne instruments such as POLDER (polarization and directionality of Earth's reflectances) provide multidirectional estimates of the surface reflectance (after atmospheric correction). A better description of the surface cover is needed for an improvement in climate modeling. This paper describes how the inversion of a three-parameter bidirectional model from the measurements yields some variables of interest such as the surface albedo, the leaf area index, the fraction of vegetation, and the daily integrated photosynthetically active radiation absorption. Airborne measurements of POLDER were made during the HAPEX-Sahel experiment over various surface types and for different atmospheric conditions. These measurements together with some "ground truth" allow a validation of the proposed method. The reflectance bidirectional signature of the Sahelian landscape shows some classical features such as a general increase toward backscattering and the hot spot phenomenon. The bidirectional model allows an accurate representation of the observed signatures. However, a large range of angular measurements is necessary to constrain the model inversion and to decrease the uncertainty in the three-parameter retrieval. The surface variables derived from these three parameters are found to be in agreement with the in situ measurements. Obviously, a validation on other landscapes with a higher vegetation coverage is now needed. The technique described in this paper will be applied to the spaceborne POLDER data sets.

1. Introduction

The atmosphere/land fluxes have a large influence on climate [*Dickinson*, 1983; *Mintz*, 1984; *Sellers*, 1985]. It has been shown that albedo variations may induce significant changes in the large-scale circulation and rainfall, particularly over the desert areas. Consequently, vegetation feedbacks might be at the origin of the severe drought periods which have occurred regularly over the last several decades [*Charney et al.*, 1977; *Henderson-Sellers*, 1992]. In order to study the surface flux influence on climate and to improve our understanding of surface-atmosphere interactions, the Hydrologic Atmospheric Pilot Experiment in the Sahel (HAPEX-Sahel) was organized in Niger during 1992 [*Goutorbe et al.*, 1994]. Surface and atmospheric measurements were used to provide information on a local scale. The experimental strategy makes use of remotely sensed data to integrate the in situ measurements of surface mass and energy fluxes at the global circulation model (GCM) grid scale.

If the GCM physical parameterizations can handle a detailed description of the surface characteristics, the present satellite-derived variables do not have the same level of quality or detail. The main parameter controlling the fluxes is the surface albedo. Current estimations are derived from observations of the advanced very high resolution radiometer (AVHRR) sensor onboard the NOAA series. These instruments provide spectral and bidirectional reflectances, when the integration over the hemisphere and the solar spectral band is a difficult task. The next generation of sensors aboard polar platforms will be very helpful in this regard. For instance, the polarization and directionality of Earth's reflectances (POLDER) instrument [*Deschamps et al.*, 1994], onboard the ADEOS (Advanced Earth Observing Satellite) launched in August 1996, acquires multidirectional reflectance measurements, which can be used for an accurate directional integration using a surface bidirectional model [*Walthall et al.*, 1985; *Kimes and Sellers*, 1985; *Kimes et al.*, 1987; *Roujean et al.*, 1992]. Moreover, the sampling of the bidirectional reflectance distribution function (BRDF) with POLDER measurements may be sufficient to invert surface reflectance models and thus to estimate additional structural parameters of the surface.

In this paper, we attempt such an approach using airborne measurements of POLDER acquired during HAPEX-Sahel. The directional characteristics of the surface reflectance are derived from the measurements after atmospheric correction. The corrected bidirectional reflectances are then inverted using the *Roujean et al.* [1992] model. The inversion results are used both to provide a hemispheric integration and to simulate the reflectances, in particular geometry, which are favorable for an estimate of surface parameters. These parameters are the fractional vegetation cover, the leaf area index (LAI), the fraction f_{APAR} of absorbed photosynthetically active radiation (APAR), and the aerodynamic roughness. The available ground truth measurements collected during the HAPEX-Sahel field campaign provide the necessary database to validate the approach.

[1]Météo France/Centre National de la Recherche Scientifique, Toulouse, France.
[2]Laboratoire d'Optique Atmosphérique/Université des Sciences et Techniques de Lille, Villeneuve d'Ascq, France.
[3]Commissariat à l'Energie Atomique/Laboratoire de Modélisation du Climat et de l'Environnement, Gif sur Yvette, France.

Paper number 97JD00341.
0148-0227/97/97JD-00341$09.00

In section 2, we describe and discuss the methods which are used to derive surface parameters from multidirectional reflectance measurements. The airborne and surface measurements are analyzed in section 3. In section 4, the inversion methods are applied to the airborne measurements, and their results are compared to ground truth data. Section 5 provides a summary and a discussion.

2. Theoretical Formulation of Inverse Problem

2.1. Bidirectional Reflectance Model of the Surface

In semiarid regions, vegetation is distributed as isolated clumps with large interstices of bare soil. Such a landscape is well adapted to the hypothesis of the reflectance model of *Roujean et al.* [1992] which considers a random distribution of vertical protrusions in assuming no mutual shadowing between them. In this model, the reflectance directional signature is described as

$$\rho(\theta_s,\theta_v,\phi)=k_0+k_1 f_1(\theta_s,\theta_v,\phi)+k_2 f_2(\theta_s,\theta_v,\phi) \quad (1)$$

where

$$f_1(\theta_s,\theta_v,\phi)=\frac{1}{2\pi}\left[(\pi-\phi)\cos\phi+\sin\phi\right]tg\theta_s tg\theta_v$$

$$-\frac{1}{\pi}\left(tg\theta_s+tg\theta_v+\sqrt{tg^2\theta_s+tg^2\theta_v-2tg\theta_s tg\theta_v\cos\phi}\right) \quad (2)$$

$$f_2(\theta_s,\theta_v,\phi)=\frac{4}{3\pi}\frac{1}{\cos\theta_s+\cos\theta_v}\left[\left(\frac{\pi}{2}-\xi\right)\cos\xi+\sin\xi\right]-\frac{1}{3} \quad (3)$$

In these equations, θ_s and θ_v are the Sun and view zenith angles, and ϕ is the relative azimuth between the Sun and the view directions. The three parameters k_0, k_1, and k_2 are surface dependent and can be inverted from the multidirectional measurements. On the other hand, the two kernels f_1 and f_2 have been derived from theoretical considerations with the constraint that they vanish for $\theta_s=\theta_v=0$. Therefore k_0 is equivalent to the nadir reflectance when the Sun is at zenith. Parameters k_1 and k_2 provide a quantification of the reflectance directional signature. f_1 has been derived using a representation of the vegetation composed of isolated protrusions over a flat surface with the same isotropic reflectance. On the other hand, f_2 assumes an infinite layer of randomly distributed leaves. Therefore k_1 can be considered as a coefficient of surface roughness, when k_2 depends on volume scattering. A hypothesis of the model is that the directional signatures resulting from the two model processes can be simply added. The model has been validated against in situ measurements [*Roujean et al.*, 1992], and successfully applied to time series of NOAA/AVHRR data [*Leroy and Roujean*, 1994]. The retrieval of the $k_{i=0,1,2}$ parameters is achieved using the standard technique of minimizing the squared difference between measurements and modeled reflectances:

$$\begin{bmatrix}\langle\rho\rangle\\ \langle\rho f_1\rangle\\ \langle\rho f_2\rangle\end{bmatrix}=\begin{bmatrix}1 & \langle f_1\rangle & \langle f_2\rangle\\ \langle f_1\rangle & \langle f_1^2\rangle & \langle f_1 f_2\rangle\\ \langle f_2\rangle & \langle f_1 f_2\rangle & \langle f_2^2\rangle\end{bmatrix}\begin{bmatrix}k_0\\ k_1\\ k_2\end{bmatrix}=\left[M(f_1,f_2)\right]\begin{bmatrix}k_0\\ k_1\\ k_2\end{bmatrix} \quad (4)$$

The determinant of the M matrix is given by

$$\det(M)=\mathrm{var}(f_1)\mathrm{var}(f_2)-\mathrm{covar}^2(f_1,f_2)=\sigma_1^2\,\sigma_2^2\,(1-r^2) \quad (5)$$

In equation (5), σ_1 and σ_2 are the standard deviations for f_1 and f_2, respectively, and r^2 is the coefficient of determination between f_1 and f_2. If f_1 and f_2 are correlated for the set of available geometry, or show very small variations, then det(M) is small and the inverted parameters $k_{i=0,1,2}$ are imprecise. Therefore det(M) is a criterion for the quality of the inversion.

2.2. Surface Albedo

The surface albedo, or hemispherical reflectance, is the integration of the reflectance over the upper hemisphere. Thanks to the model linear formulation, the inverted parameters yield an easy estimate of the surface albedo. The numerical integration over the upper hemisphere of the kernels f_1 and f_2 was achieved by *Roujean et al.* [1992]. The surface albedo is derived from

$$a(\theta_s)=\frac{2}{\pi}\int_0^{\pi}d\phi\int_0^{\pi/2}\rho\cos\theta_v\sin\theta_v d\theta_v=k_0+k_1 I_1(\theta_s)+k_2 I_2(\theta_s) \quad (6)$$

where

$$I_1=-0.9946-0.0281\,tg\,\theta_s-0.0916\,tg^2\theta_s+0.0108\,tg^3\theta_s \quad (7)$$

$$I_2=-0.0137+0.0370\,tg\,\theta_s+0.0310\,tg^2\theta_s-0.0059\,tg^3\theta_s. \quad (8)$$

I_1 and I_2 have been derived from a fit with the numerical integration of the functions f_1 and f_2, respectively. I_1 accounts for the effect of shading by protrusions of adjacent open areas and I_2 for light trapping by the "microstructure" of the vegetation (leaves, branches). I_2 increases with the Sun angle, while I_1 decreases because of the enhanced portion of shaded surfaces. Note that I_1 and I_2 provide a directional albedo. An integration of these functions over the hemisphere provides an estimate of the diffuse albedo.

Note that the functions above are valid only in the spectral bands for which they have been measured. GCMs, on the other hand, need a value integrated over the solar spectrum. The broadband albedo A is often estimated from the visible albedo A_{VIS} and the near infrared albedo A_{NIR} using the relationship for vegetated surfaces given by *Wydick et al.* [1987] for AVHRR channels :

$$A = 0.36\,A_{VIS} + 0.73\,A_{NIR} - 0.7 \quad [\%]. \quad (9)$$

2.3. Fraction of Vegetation

The fraction of vegetation σ_f as defined by *Deardorff* [1978] is a key parameter for the boundary layer parameterizations. It quantifies the relative fractions of bare soil and vegetation and is necessary to evaluate water and energy fluxes at the surface. It is now used in most land surface parameterization schemes such as the biosphere-atmosphere transfer scheme (BATS) [*Dickinson*, 1983; *Dickinson et al.*, 1986], the simple biosphere model (SiB) [*Sellers et al.*, 1986; *Sato et al.*, 1989], and the interaction surface biosphere atmosphere (ISBA) scheme [*Noilhan and Planton*, 1989].

To estimate this parameter from bidirectional reflectance measurements, we assume that the landscape is composed of bare soil and dense vegetation. When the Sun and the observer are both at zenith, σ_f is equivalent to the fraction of solar radiation intercepted by the vegetation [*Smith et al.*, 1993]. For this observation geometry the predicted reflectance is k_0. Therefore

$$k_0=\sigma_f\rho_{veg}+(1-\sigma_f)\,\rho_{soil}=(\rho_{veg}-\rho_{soil})\,\sigma_f+\rho_{soil} \qquad (10)$$

where ρ_{veg} is the vegetation reflectance, and ρ_{soil} is the soil reflectance.

In order to minimize the soil reflectance uncertainty, we use the difference vegetation index $(DVI)_0$:

$$(DVI)_0=(k_0)_{864}-(k_0)_{670}$$

$$(DVI)_0=\left[(\rho_{veg}-\rho_{soil})_{864}-(\rho_{veg}-\rho_{soil})_{670}\right]\sigma_f+(\rho_{soil})_{864}-(\rho_{soil})_{670}$$

$$(DVI)_0=0.442\,\sigma_f+0.046 \qquad (11)$$

The numerical values in (11) were determined from an empirical fit in using the data collected by *Kimes* [1983] and *Kimes et al.* [1985, 1986] over a large range of canopies [see *Roujean et al.*, 1992, Table 1]. This evaluation procedure yields a coefficient of determination R^2 of 0.85. The offset in the relationship is coherent with the typical reflectance increase of bare soil from 670 nm to 864 nm. Similarly, a $(DVI)_0$ of 0.49 for a fully covering vegetation agrees with the typical spectral signature of vegetation.

2.4. Leaf Area Index

The leaf area index (LAI) is also an important parameter, controlling physical, biological, and hydrological processes of plant canopies. In this paper, we estimate the LAI through f_{IPAR} which is the fraction of intercepted PAR

$$f_{IPAR}=1-exp\left(-b\frac{G(\theta_s)}{\mu_s}LAI_e\right) \qquad (12)$$

where b is the backscattered fraction, $LAI_e=\lambda_0 LAI$ is the effective LAI [*Chen and Black*, 1991] with λ_0 being the clumping index, and $G(\theta_s)$ is the leaf projection factor [*Ross*, 1981]. For a LAI retrieval, some parameters in (12) need to be fixed arbitrarily, while the resulting uncertainty can be minimized using directional measurements. Among them, b characterizes the spectral dependence [see *Sagan and Pollack*, 1967],

$$b\approx 1-\omega\frac{g+1}{2}, \qquad (13)$$

including the leaf albedo $\omega=r+t$, where r is leaf reflectance and t is leaf transmittance, and the asymmetry factor g which ranges from -1 (for complete backscattering) to 1 (for complete forward scattering). For random canopies, g takes the form

$$g=-\frac{4}{9}\frac{r-t}{\omega} \qquad (14)$$

At this stage, some discussion is necessary about the clumping of vegetation and its effect on the radiative transfer modeling. *Nilson* [1971] first introduced a clumping index λ_0 to account for the degree of dependence of the positions of the vegetation stands; λ_0 is greater than 1 for a regular dispersion, as in rows; $\lambda_0=1$ for a random dispersion, and $\lambda_0<1$ for a clumped dispersion. Clumping increases the fraction of radiation reaching the surface. Consequently, the LAI may be underestimated if randomness is assumed when using a LAI-reflectance relationship similar to (12). The sensitivity of the LAI-reflectance relationship to clumping varies with the observation geometry. *Rowe* [1993] notes that when the Sun is at zenith, there is no shading by adjacent open areas, and interception is solely reduced by light trapping into bushes. Also, *Bégué* [1992] found that the extinction coefficient is independent of the clump shape for a Sun at zenith. On the other hand, oblique measurements have the advantage of reducing the effect of the uncertainty on G. However, our strategy makes use of nadir observations, taking advantage of available measurements for G. This choice is made because the retrieval of k_0 is more accurate than that of k_1 and k_2. Then, considering that $\sigma_f=f_{IPAR}(\theta_s=0°)$, equations (11) and (12) yield

$$LAI=\frac{LAI_e}{\lambda_0}=-\frac{\ln(1-\sigma_f)}{b\,G(\theta_s=0°)\lambda_0}=-\frac{\ln\left[1-\dfrac{(DVI)_0-0.046}{0.442}\right]}{b\,G(\theta_s=0)\lambda_0}. \qquad (15)$$

2.5. Fraction of Absorbed PAR

The fraction f_{APAR} of absorbed photosynthetically active radiation by plants is a key parameter for quantitative assessments of the primary production and global atmospheric CO_2 budget [*Fung et al.*, 1987; *Prince*, 1991]. It is also useful to derive estimates of the canopy stomatal resistance and photosynthesis rate for which it constitutes an important limiting factor [e.g., *Sellers*, 1985]. The quantity of interest is the f_{APAR} not limited to the time of observation, but that integrated over the whole day, that is the daily fraction $\overline{f_{APAR}}$. Assuming that daily integration of $G(\theta_S)/\mu_S$ is close to 1, the quantity $\overline{f_{APAR}}$ is the daily portion $\overline{f_{IPAR}}$ of radiation interception expressed in (12) that is not reflected, and where possible reflection by soil background is considered; that is,

$$\overline{f_{APAR}}=\overline{f_{IPAR}}-\rho+\rho_{soil}(1-\overline{f_{IPAR}}) \qquad (16)$$

Statistical relationships have been proposed to relate $\overline{f_{APAR}}$ to spectral vegetation indices such as the normalized difference vegetation index (NDVI) obtained from instantaneous measurements [*Kumar and Monteith*, 1981; *Asrar et al.*, 1984; *Sellers*, 1987; *Goward and Huemmrich*, 1992; *Myneni and Williams*, 1994]. However, these relationships may significantly differ because NDVI is affected by soil spectral properties, vegetation geometry, and Sun/view angle effects. *Roujean and Bréon* [1995] recommend from theoretical considerations to use for the optimum geometry (θ_s=45°, θ_v=60°, ϕ=0°) the renormalized difference vegetation index (RDVI) defined as

$$RDVI=\frac{\rho_{864}-\rho_{670}}{\sqrt{\rho_{864}+\rho_{670}}}. \qquad (17)$$

Therefore

$$(\mathrm{RDVI})_{opt} = 0.552\ \overline{f_{APAR}} + 0.116 \qquad (18)$$

where $(\mathrm{RDVI})_{opt}$ is estimated from the reflectances of (17) obtained in the optimum geometry. The optimum spectral reflectances $(\rho_{opt})_\lambda$, where λ stands for 670 or 864, are calculated as

$$(\rho_{opt})_\lambda = (k_0)_\lambda - 0.240(k_1)_\lambda + 0.202(k_2)_\lambda . \qquad (19)$$

The RDVI was found to be quite equivalent to the soil-adjusted vegetation index (SAVI), which is a suitable index to study semiarid landscapes because it is more efficient than the NDVI in reducing the soil background effect [*Huete*, 1988].

2.6. Aerodynamic Roughness

The estimate of a heterogeneity scale (or roughness) is necessary for climate modeling because of its influence on the turbulence and momentum flux in the boundary layer. Some roughness parameters have been defined in the optical remote sensing community, as in the works of *Otterman and Tucker* [1985] or *Roujean et al.* [1992]. The dimensionless protrusion parameter k_1/k_0 (see (1)), based on the averaged height and distance of the clumps [see *Roujean et al.*, 1992] quantifies the surface roughness and is well adapted to the Sahelian vegetation structure. Because the leaf reflectance is small in the visible. there is little multiple reflections, and shadowing effects are dominant. On the other hand, measurements at 670 nm are better adapted than those at 864 nm because the fraction of direct radiation, as opposed to diffuse, is then larger. This is why the 670 nm measurements are preferred to measure the surface roughness. However, the roughness, which is accessible through optical remote sensing, is a dimensionless parameter which differs from the aerodynamic and thermal roughness lengths used in climate modeling. Still, we attempt here to give an estimate of the aerodynamic roughness-parameter z_0 involved in climate modeling from the formula of *Lettau* [1969]. This formula includes an optical roughness equivalent to our protrusion parameter at 670 nm :

$$z_0 = 0.5\,(h^*)(k_1/k_0)_{670} \qquad (20)$$

where h^* is the average vertical extent, and 0.5 is an average drag coefficient of the characteristic individual obstacle. After *Lettau* [1969], such an approach is expected to agree within about ±25%, from the results of detailed analysis of measured wind profiles.

3. Measurements during HAPEX-Sahel

3.1. Surface Characteristics

The Central West supersite (15 km x 15 km) of the HAPEX-Sahel experiment [e.g. , *Goutorbe et al.*, 1994] includes four specific sites with various vegetation covers typical of the sahelian landscape: a grass fallow, a shrub fallow, a millet crop, and a degraded shrubland. The three former vegetation units are considered in this study. The degraded shrubland is a "Guiera Senegalensis" shrub, consisting of two distinct components, a discontinuous upper story of bushes and a sparse understory of grass. The shrub fallow includes a continuous grass layer. The millet crop is a clumped canopy which started to grow up around mid-July. These sites were equipped with a set of sensors which continuously measured, at the surface, the transmitted PAR and near infrared fluxes during the rainy season [*Bégué et al.*, 1996a]. Other sensors were positioned a few meters above the bushes to measure their hemispherical reflectance (albedo). These measurements allowed an estimate of $\overline{f_{APAR}}$ as well as an accurate characterization of the radiative transfer within the canopy to be used for the understanding and interpretation of remotely sensed data.

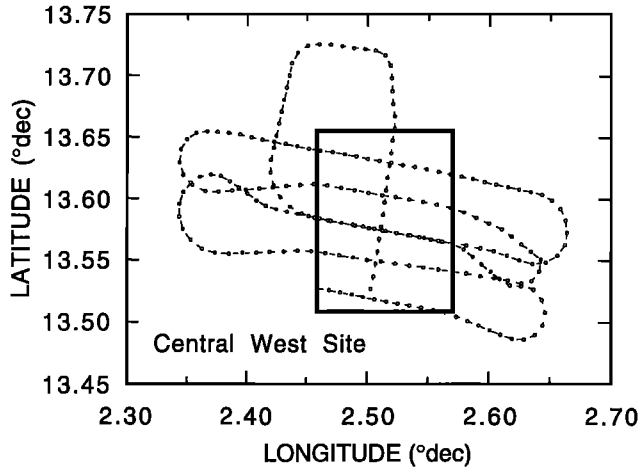

Figure 1. A typical POLDER flight over the Central West site. The rectangle indicates the useful part of the flight.

The LAI was measured during the growing season by nondestructive measurements on the selected sites and harvest measurements at places close to the experimental sites [*Bégué et al.*, 1996b]. The measurements were then extrapolated in time with a logistic-type function and to a larger space scale of 300 x 300 m^2 as described by *Bégué et al.* [1996b].

Shrub fallow is highly representative of sahelian vegetation. The leaves are organized into bushes which can be arranged in a variety of patterns, most frequently as clumps. The soil shows a rather high albedo, of the order of 0.25 in the PAR and 0.4 in the near infrared [*Bégué et al.*, 1996b], and this clumped canopy is expected to have a higher albedo than that of the leaves.

Table 1. Summary of POLDER Flights

Day	Site	Time Flight
Aug. 24	Central West	0925-1000
Sept. 3	Central West and East	1445-1605
Sept. 6	Central West and South	1425-1515
Sept. 13	Central West	1440-1520
Sept. 17	Central West	1450-1530
Sept. 29	Central West	0730-0815
Oct. 2	Central West	0750-0835
Oct. 4	Central West	0755-0840

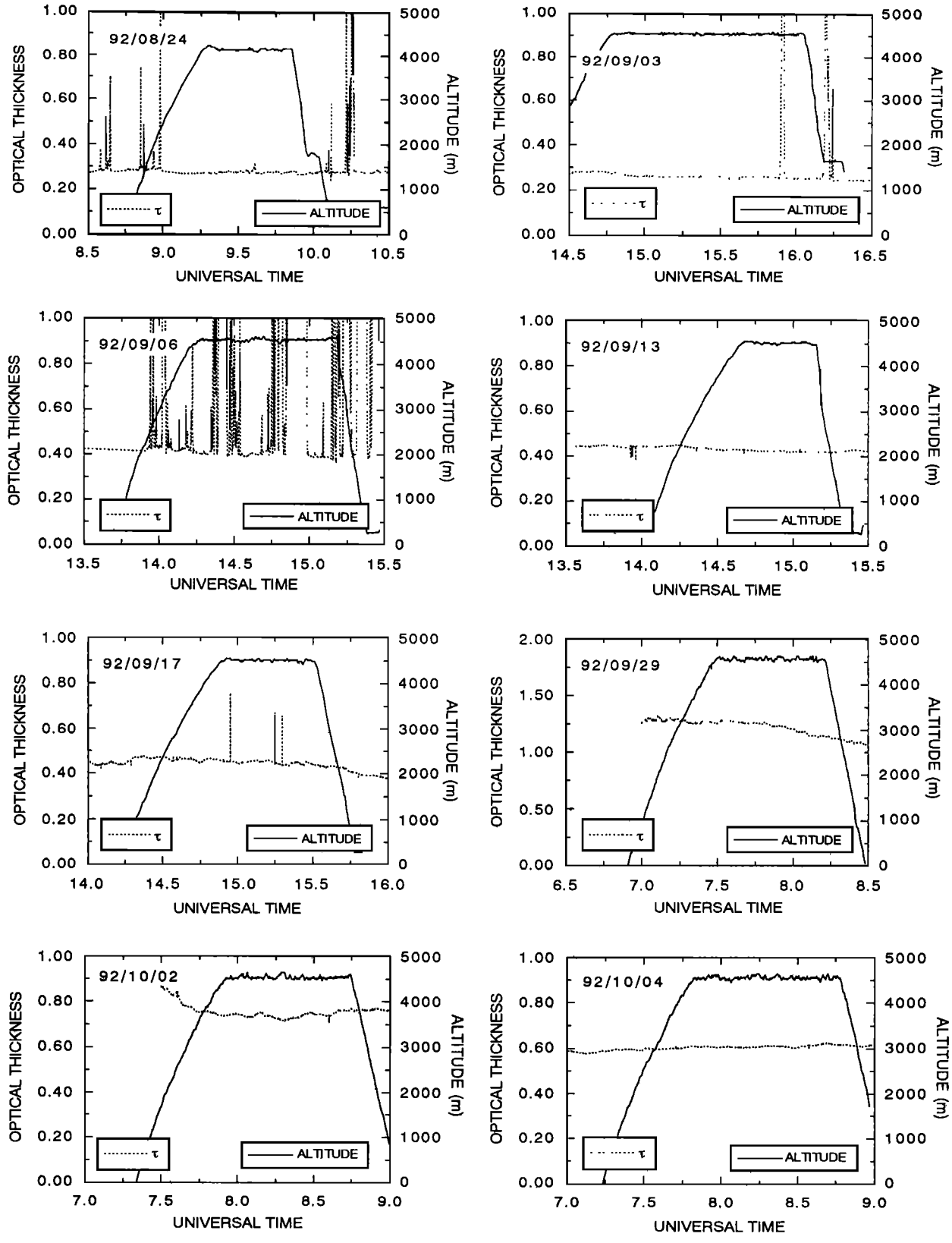

Figure 2. Time evolution of the aerosol optical thickness (left axis) at 450 nm for the eight POLDER flights. The aircraft altitude is also reported (right axis).

Table 2. Aerosol Optical Thickness Measured in Several Spectral Bands during POLDER flights

Day	Time	τ_{450}	τ_{550}	τ_{680}	τ_{870}	τ_{1050}	τ_{1250}	τ_{1610}	α_{vis}	α_{nir}	$\Delta\tau_{870}$
Aug. 24	0750-1010	0.260	0.245	0.228	0.221	0.184	0.178	0.159	0.24	0.55	0.006
Sept. 3	1400-1530	0.276	0.259	0.241	0.220	0.196	0.193	0.150	0.34	0.64	0.011
	1530-1720	0.248	0.230	0.214	0.194	0.173	0.169	0.122	0.37	0.78	0.008
Sept. 13	1300-1730	0.429	0.422	0.412	0.394	0.370	0.354	0.279	0.13	0.57	0.014
Sept. 17	1410-1540	0.475	0.456	0.440	0.413	0.383	0.366	0.277	0.21	0.66	0.013
Sept. 29	0700-0800	1.309	1.272	1.206	1.136	1.040	0.959	0.793	0.21	0.60	0.019
Oct. 4	0630-1000	0.630	0.616	0.593	0.562	0.522	0.484	0.385	0.17	0.63	0.011

The Angstroëm coefficient α_{vis} is derived from 450 nm and 870 nm measurements, whereas α_{nir} is computed from 870 nm and 1610 nm. $\Delta\tau_{870}$ is the standard deviation of τ_{870} during the indicated time period.

3.2. Airborne POLDER Measurements

The POLDER instrument has been developed at the "Laboratoire d'Optique Atmosphérique" for the measurement of directional and polarization signatures of the Earth reflectances. It is based on the concept of a CCD matrix array detector, a rotating wheel which carries filters and polarizers and a wide field of view lens. The spectral bands are 443, 570, 670, 864, and 910 nm. For two of these bands (443 and 864 nm) a polarizer is added to the filters. The optics allow a total field of view of 114°, with maximum viewing angle along track and cross track of 43° and 51°, respectively. One measurement, for each spectral band, is acquired every 10 s. The airborne instrument is very similar to the spaceborne instrument, described in detail by *Deschamps et al.* [1994]. A presentation of the airborne instrument, the data acquisition procedure, and the first results from land surface observations appear in the work of *Deuzé et al.* [1993].

The POLDER digital counts are first converted to reflectances using calibration coefficients derived from laboratory measurements achieved before and after the field experiment. The accuracy is expected to be of the order of 5%. The noise equivalent reflectance due to radiometric noise is about 0.003.

In order to obtain an adequate sampling of the BRDF of a given target, a typical POLDER flight plan consists of five flight lines parallel to the Sun direction and another perpendicular to it. Figure 1 illustrates a typical pattern performed on September 29 over the Central West site. The nominal flight altitude was 4500 m, which yield a ground pixel size of about 25 m. Each flight line was 15 km long, and the distance between them was 2 km. With such geometry, any surface target on the central subtract is observed from any of the flight lines with varying viewing angles. Table 1 indicates the main target and time for each flight. It shows that the Central West site was the main target, due to the availability of concomitant surface measurements.

3.3. Atmospheric Conditions

The climate over the experimental area varies greatly with the position of the Intertropical Convergence Zone (ITCZ). During August the study area was under the influence of moist air masses (rainy season), whereas September was the beginning of the dry season induced by a southern shift of the ITCZ. During the dry season the wind is usually blowing from the north east (harmattan) and is associated with dust transport. During the rainy season the wind blows from the south west, and the air masses generally show a low turbidity, except when dust storms precede local thunderstorms. The turbidity conditions measured by ground-based Sun photometers were very variable during the experiment (Table 2). From August 24 to mid-September, only 9 days were cloud free to allow Sun observations. The mean optical thickness was around 0.30 with extreme values of 0.28 and 0.43 at 450 nm. From mid-September to mid-October the atmosphere was dustier with a mean optical thickness of 0.7 with extreme values of 0.48 and 1.31.

Figure 2 shows the aircraft altitude during the eight POLDER flights as well as the concomitant turbidity conditions expressed by the aerosol optical thickness measured at 450 nm (τ_{450}). The large fluctuations in the optical thickness values observed on September 6 result from cloudiness. On September 29 the optical thickness was so high (τ_{450}~1.3) that the surface was not visible from flight altitude. The flight of October 2 has not been analyzed because of a lack of surface-based atmospheric optical measurements.

During the experiment the aerosol optical properties were monitored through the measurements of the following quantities: the spectral optical thickness (between 400 nm and 2200 nm), sky radiance, and polarization state at 864 nm and 1650 nm. From these measurements the aerosol optical and physical properties were derived [*Devaux et al.*, 1989; *Tanré et al.*, 1988]. An example of an aerosol phase function, derived from the atmospheric optical measurements, is given in Figure 3. The spectral aerosol optical thicknesses for the POLDER flights are reported in Table 2.

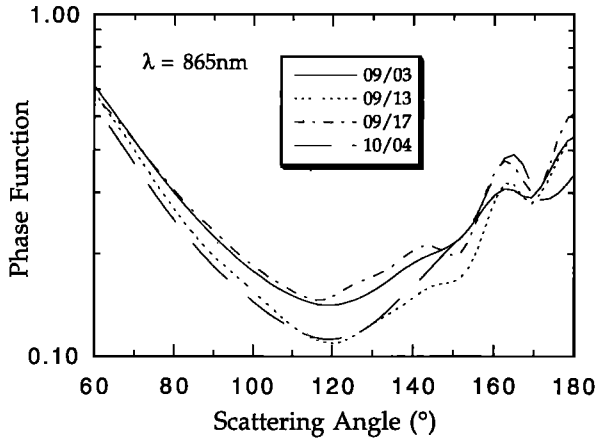

Figure 3. Aerosol phase functions at 865 nm for the four POLDER flights. The phase function measured on August 24 is very similar to that of September 17 and is not reported here.

3.4. Atmospheric Correction

Remote sensing of surface properties from spaceborne or airborne instruments is affected by the presence of the atmospheric layer. The measured reflectance ρ^* is related to the surface reflectance ρ by [e.g., *Tanré et al.*, 1979; *Fraser and Kaufman*, 1985; *Lee and Kaufman*, 1986] :

$$\rho^*(\theta_s,\theta_v,\phi)=\rho_a+\frac{\rho T(\theta_s)T(\theta_v)}{1-\rho S} \quad (21)$$

where $\rho_a(\theta_v, \theta_s, \phi)$ is the atmospheric reflectance, $T(\theta_s)$ is the atmospheric downward transmission (Sun to surface), $T(\theta_v)$ is the upward transmission (surface to instrument), and S is the atmospheric spherical albedo. In addition to the geometrical conditions, the various parameters in (21) depend on the aerosol optical properties which are derived from the atmospheric optical measurements (Figure 3). They are computed by solving the radiative transfer equation with an algorithm based on the successive orders of the scattering method [*Lenoble*, 1993].

Water vapor absorption in the POLDER spectral bands is negligible. On the other hand, ozone absorption has a significant impact on the 670 nm channel, which is corrected using climatological ozone amounts. As for the aerosol effect, the transmission and reflectance of the aerosol layer is accounted for, but the coupling between surface directional effects and atmospheric scattering is neglected. A full atmospheric correction would necessitate multiple iteration of surface BRDF estimate and atmospheric radiative transfer calculations. We consider that since most of the radiance scattered by aerosol is little deviated (forward peak of the phase function), the blurring of the surface BRDF is small. Plates 1 and 2 illustrate the impact of the atmospheric correction scheme for the flights of September 3 and October 4 at 864 nm. These are the clearest and dustiest days. Plate 1a corresponds to the airborne measurements (before any atmospheric corrections), and Plate 1b corresponds to the same image after correction. The two quantities, which are applied to the raw data following (21) for correction (path radiance and transmission function), are reported in Plate 1c and 1d. If images Plates 1a and 1b are quite similar on September 3, the results for October 4 show the importance of atmospheric correction for significant optical thicknesses. The correction is a function of the viewing geometry and therefore of the pixel position in the image. Note that the relative importance of atmospheric correction is even larger in the visible channels since the atmospheric optical thickness is larger, and the surface reflectance is smaller than in the near infrared.

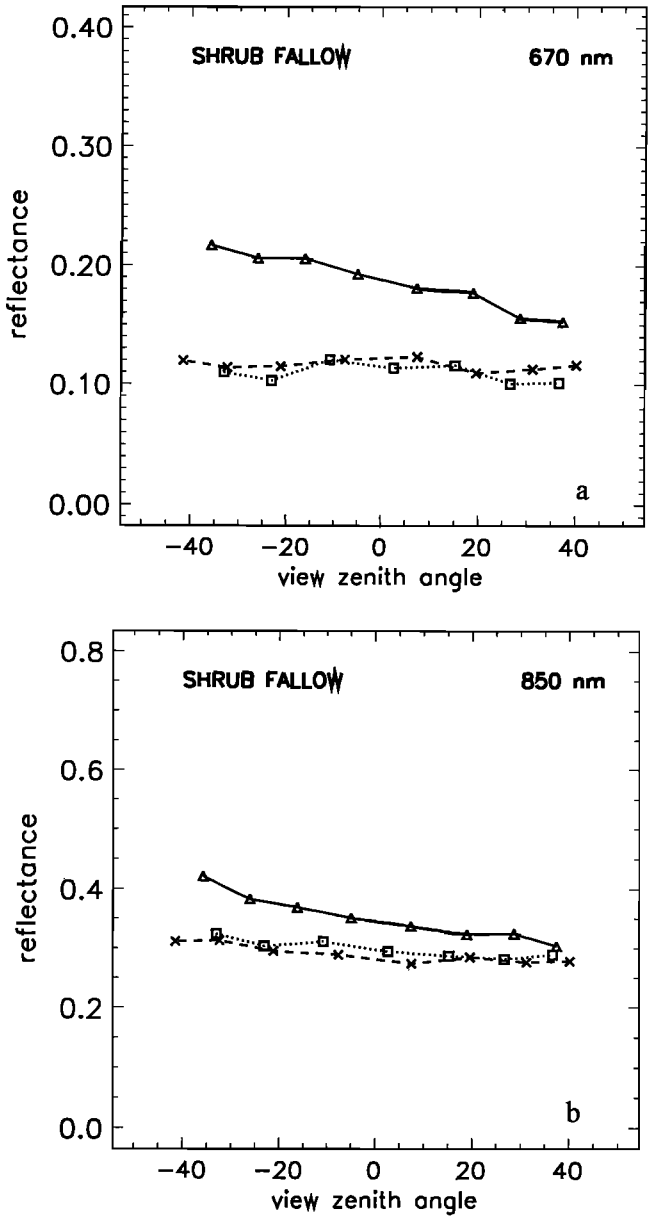

Figure 4. Shrub fallow bidirectional reflectance for an azimuth ϕ close to the principal plane, as estimated from POLDER measurements on August 24 (triangles, dashed) with (θ_s=34.7°, ϕ=12°), September 17 (squares, dotted) with (θ_s=52.5°, ϕ=20°), and on October 4 (crosses, dashed) with (θ_s=54.8°, ϕ=5°). Positive (negative) θ_v corresponds to the forward (backward) direction. (a) 670 nm; (b) 864 nm.

4. Results

4.1. Angular Signatures of Sahelian Vegetation

Figures 4a and 4b show the surface bidirectional reflectance of shrub fallow observed close to the principal plane at 670 nm and 864 nm, respectively, on August 24, September 17, and October 4. The Sun zenith angle is 34.7° on August 24 and around 50° for the other two days. Large bidirectional effects are observed at the beginning of the growing season at 670 nm: the reflectance varies from 0.15 in forward scattering up to 0.22 in backscattering. At 864 nm the reflectance increase is about 0.08 from nadir to 40° off nadir. A similar directional signature was observed over millet crop (not shown) with larger bidirectional effects. As the vegetation grows, the surface reflectances become more isotropic. This result seems to be due to neglecting the coupling between surface and atmospheric effects which becomes more important along the season with the enhanced atmospheric optical thickness.

The hot spot phenomenon is a reflectance directional signature of particular interest since several theoretical studies show that it is very sensitive to the vegetation small-scale structure [*Kuusk*, 1985; *Hapke*, 1986; *Jupp and Strahler*, 1991].

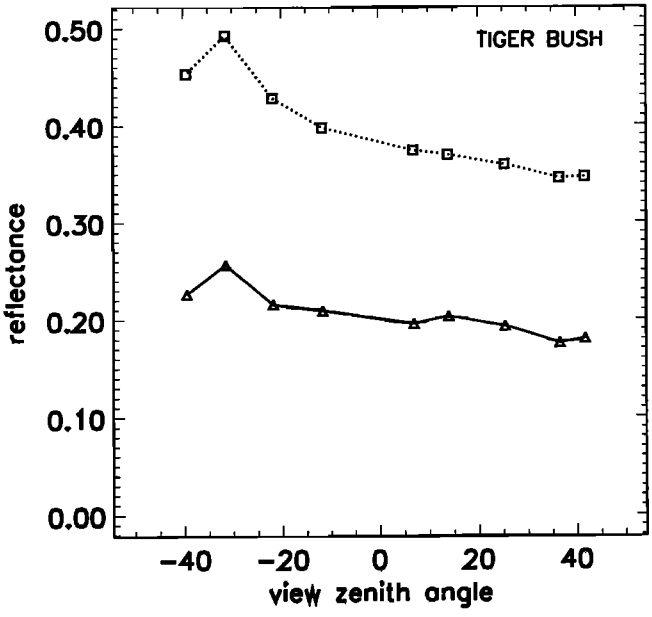

Figure 5. Tiger bush bidirectional reflectance in the principal plane, as estimated from POLDER measurements at 670 nm (triangles, dashed) and at 864 nm (squares, dotted).

Figure 5 shows the reflectance observed in the principal plane on August 24 over a tiger bush target located in the southern part of the Central West site. The size of the target is about 30,000 m² (7 x 7 pixels) which is about the scale of homogeneity of such vegetation. The hot spot effect yields a reflectance increase from 0.35 (forward scattering direction) to 0.5 (backscattering direction) at 864 nm. In the visible (670 nm) the reflectance increase is from 0.18 to 0.25. The bottom image in Plate 3 shows a POLDER acquisition over the Central West site at 864 nm on September 13. An analysis of this image confirms the importance of backscattering effects on the reflectance over sahelian landscape. These effects are smaller in the visible as indicated by the analysis of Figure 4a. Plate 3 shows a maximum of reflectance in the Sun direction (hot spot).

4.2. Directional Model Inversion

The reflectance bidirectional model (equation (1)) is applied to atmospheric corrected reflectance measurements for the three selected vegetation targets (shrub fallow, millet crop, and degraded shrubland). The results are reported in Table 3. The model allows an accurate representation of the surface directional signature, at least when the root mean square error δ_{obs} associated to the reflectance measurements is adequately small, beyond 1% in absolute units of reflectance. This could explain why the model performs, in general, better in the near infrared where bidirectional effects are relatively larger than in the visible, which is not usually the case. In the physical elaboration of the *Roujean et al.* [1992] bidirectional model, the k_1 and k_2 parameters are necessarily positive. However, the least squares inversion yields negative values for a few measurement sets, in particular when the observation set appears noisy. In such cases a physical interpretation of the retrieved parameters is impossible. For a few cases the model-measurement correlation is rather low. A careful analysis of the corresponding measurement sets indicated unrealistic directional signatures, which may result from misregistration errors.

The increase with wavelength of the corrected reflectance k_0 is coherent with the spectral signature of both soil and vegetation. The temporal variation of this parameter shows a general decrease. This results from an increased fraction, over the target, of vegetation which has a smaller reflectance than soil in both the visible and the near infrared spectral ranges.

Table 3 indicates that the kernels f_1 and f_2 are rather correlated, for the set of observation geometry, which yields instabilities on the retrieval of k_1 and k_2. This is because the many directional measurements have been acquired with a relatively small variation of Sun zenith angle; the correlation disappears for larger ranges of solar angles [*Roujean et al.*, 1992]. The relative variance $\sigma_1^2 / \overline{f_1}$ is rather stable, about -0.3 for both shrub fallow and millet, two sites well sampled by POLDER flights. On the contrary, $\sigma_2^2 / \overline{f_2}$ varies significantly between flights which shows its sensitivity to sampling.

Figures 6a and 6b show, for each selected site, the directional signature predicted by the model together with the measurements acquired on September 13. The model reflectances are computed for a solar zenith angle of 52.5° which was its mean value during the flight. These figures confirm that the three-parameter model is able to accurately reproduce the measured directional signatures. Figure 6c shows, for the same targets and measurements, the NDVI directional signature computed from both measurements and model at 670 nm and 864 nm. The relative variations of the NDVI with the observation geometry are lower than those of the reflectances (Figure 6c).

The normalized reflectance k_0 and the bidirectional parameters k_1 and k_2 retrieved from POLDER observations, are used hereinafter to estimate surface parameters with equations displayed in section 2.

4.3. Surface Albedo

Figure 7 shows the diurnal variation of the shrub fallow surface albedo derived from the retrieved BRDF with equations (6) and (9) on September 13. For (9) the AVHRR channels are replaced by the POLDER bands at 670 nm and 864 nm. The diurnal variability of the albedo is low, which confirms other studies [*Allen et al.*, 1994; *Bégué et al.*, 1996a]. The order of magnitude of the POLDER albedo is similar to the in situ measurements reported by *Bégué et al.* [1996a] for the same date, 0.12 in the PAR and 0.32 in the near infrared. The simple model of (6) indicates that the variations of I_1 and I_2 are of opposite sign which yield a small variation with solar angle. A numerical integration of (6) was carried out on days of POLDER flight, from the daily minimum of Sun zenith angle up to 65°, as this is the domain of validity of the model. The results are reported in Table 4 for the various flights during the growing season. The visible and near infrared albedo variations are of opposite signs, which yields a reduced variability of the broadband albedo of (9).

4.4. Fraction of Vegetation

The validity of (11) is verified in comparing POLDER-derived $(DVI)_0$ with in situ measurements of the fraction of vegetation σ_f for the shrub fallow and millet crop (Figure 8). Note that our set of measurements only contains vegetation types of relative low coverage. Figure 8 shows that results of measurements acquired during HAPEX-Sahel are in good

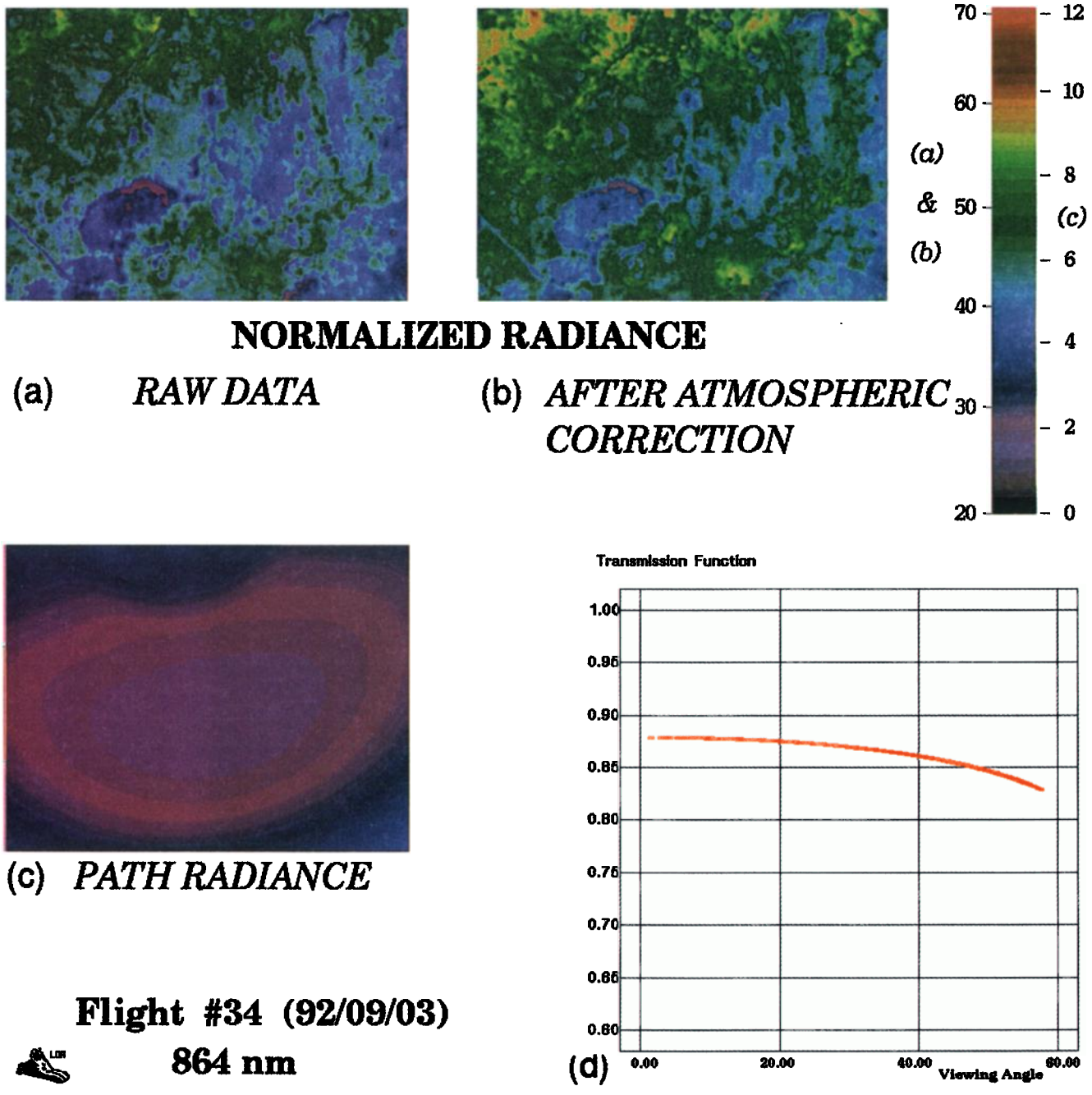

Plate 1. Typical POLDER image, acquired here at 865 nm on September 3. Plate 1a corresponds to the reflectance measurements before any atmospheric corrections and Plate 1b is for the same image after correction; (c) atmospheric reflectance, (d) atmospheric transmittance. The left side of the color scale applies to Plates 1a and 1b, and the right side to Plate 1c.

agreement with the previous analysis (see section 2.3). The relative error to calculate the fraction of vegetation using (11) is lower than 9%, while an accuracy of about 10% is needed in climate models.

4.5. Leaf Area Index

The LAI considered here includes the green LAI, the SAI (stem area index) and the WAI (wood area index) [e.g., *Bégué et al.*, 1996a]. For a LAI estimate using (15), the parameters b, G, and λ_0 are needed. Parameter b is calculated from equations (13) and (14) using in situ measurements reported in Table 5. On the other hand, G and λ_0 are derived from the analysis of the diurnal cycle of radiation interception F_{IPAR} which is modeled as

$$F_{IPAR} = (1-f)\, f_{IPAR} + f\, \overline{f_{IPAR}} \qquad (22)$$

where f is the fraction of diffuse irradiance, which was measured on the site, and $\overline{f_{IPAR}}$ is f_{IPAR} of (12) with $G(\theta_s)/\mu_s \approx 1$. Simulations of F_{IPAR} with (22) have been attempted for planophile, erectophile, and randomly oriented canopies, using

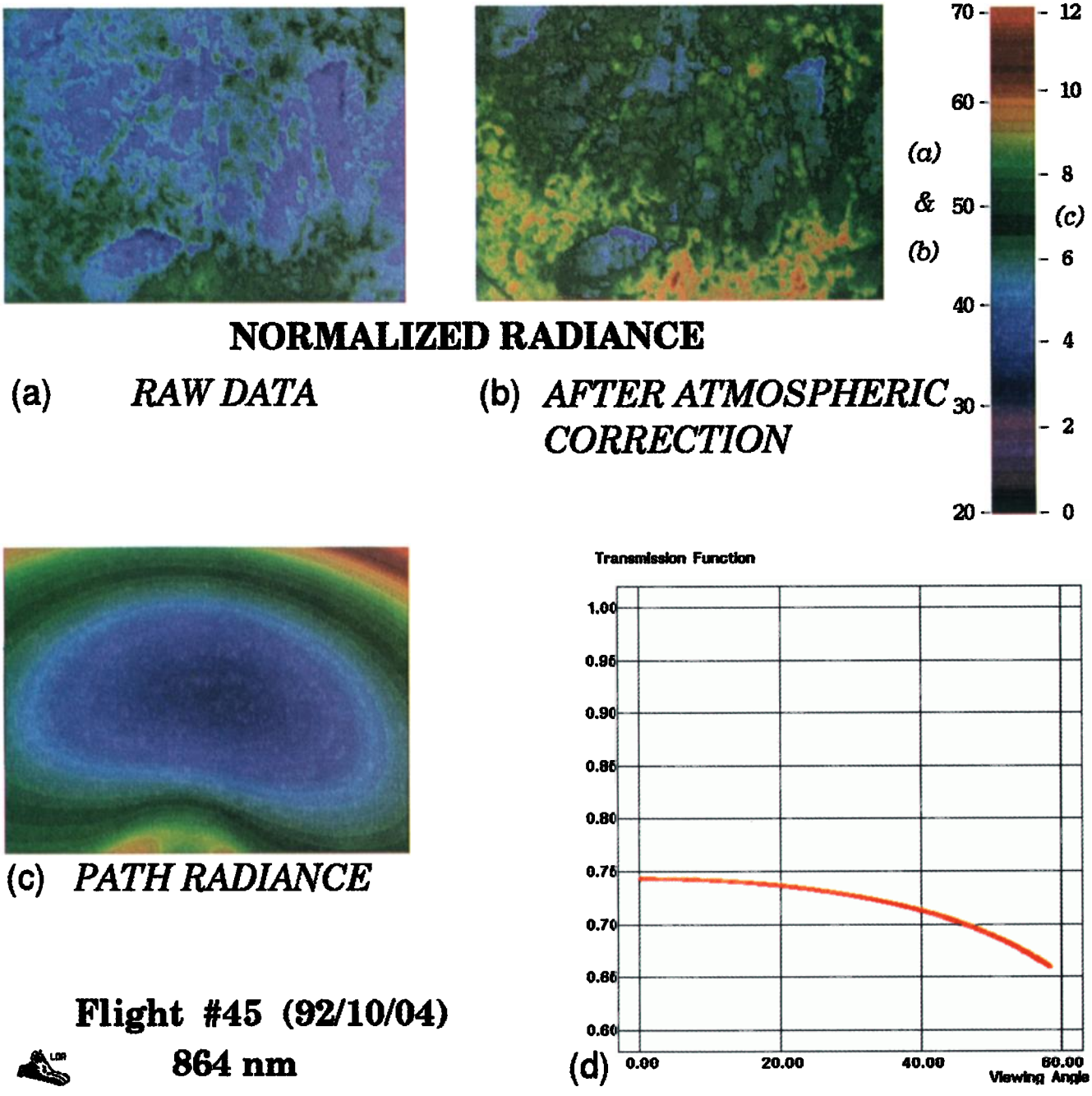

Plate 2. Same as in Plate 1 but for October 4.

measurements acquired on September 25, including a LAI value of 1.2. It is concluded from the comparison of the shapes of simulated and measured F_{IPAR} curves (Figure 9) that the shrub fallow foliage is randomly oriented, which yields G~0.5. A similar analysis lead to the same conclusion for millet. The parameter λ_0 is finally assessed in adjusting observed and modeled curves of F_{IPAR} (Figure 9), and a value of 0.71 was retrieved for shrub fallow on the sample plot. The foliage geometry and arrangement of shrubs is assumed invariant, and the estimated values for G and λ_0 are kept constant in the following studies. Moreover, the spectral properties of leaves (shown in Table 5) are kept constant, because we assume that the reflectance variations are mostly driven by vegetation growth rather than changes in the leaf spectral properties. Using these parameters (G, λ_0, and b), LAI is estimated, as shown in (15), using the σ_f values derived from POLDER data, as explained in the previous section.

The comparison between measured and POLDER-derived LAI is within 20% in relative units for shrub fallow (Figure 10). On the other hand, the procedure above cannot be successful for the millet plot because its covering did not exceed 10% over the growing season, and the reflectance data set is mostly driven by the soil spectral properties.

4.6. Daily PAR Absorbed

We compare surface measurements of the daily fraction of absorbed PAR with estimates derived from bidirectional

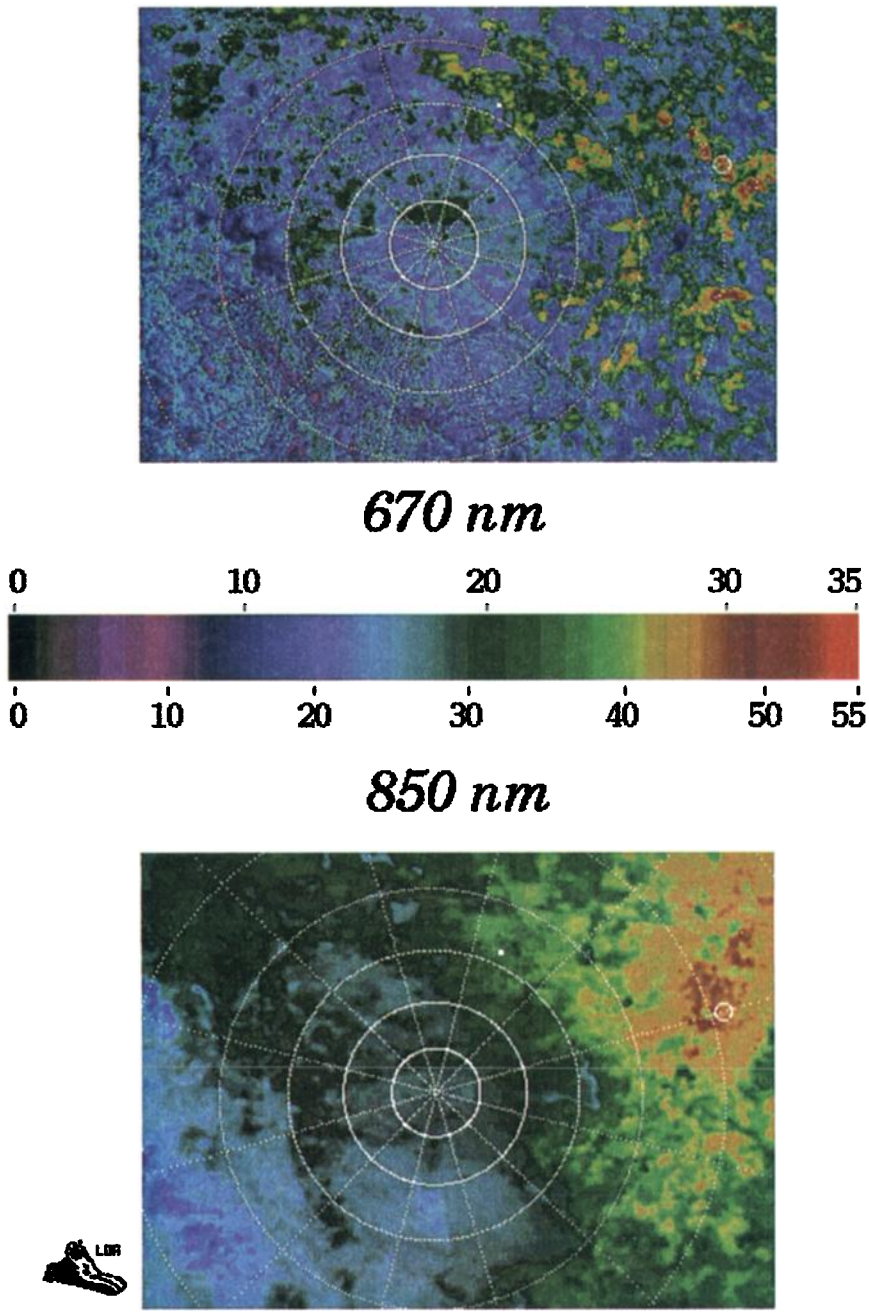

Plate 3. Typical POLDER image of the Central West site, here acquired on September 13, after atmospheric correction. The superimposed grid indicates the viewing geometry: the circles are for the view zenith angle, and the lines are for the relative azimuth between Sun and view directions. The Sun direction (i.e., that of the hot spot) is shown. The top image is for 670 nm, whereas the bottom image is for 864 nm.

measurements, as described in section 2.5. The method makes use of the reflectance measurements extrapolated to an optimum geometry using the surface bidirectional model. As for the "ground truth", hourly measurements of f_{APAR} were routinely collected on all selected sites from sunrise to sunset and averaged to derive the daily $\overline{f_{APAR}}$. Despite the uncertainty in extrapolating the measurements to a geometry which was not acquired, Figure 11 shows a satisfactory agreement between the airborne estimates and the surface measurements. A small bias is observed, however, which is probably caused by the high reflectance of sahelian soil.

4.7. Aerodynamic Roughness

The protrusion parameter $(k_1/k_0)_{670}$ is given in Table 4 for each POLDER flight day. At 670 nm, this protrusion parameter is about 0.36 on shrub fallow, and 0.2 for millet. The surface roughness z_0 is estimated as in (20) using in situ measurements of the vegetation vertical extent h^* of 150 cm for shrubs and 118 cm for millet at maturity. The estimate for shrub fallow on October 4 is much lower than that of earlier days. This is unrealistic and results probably from errors in atmospheric correction (the large optical thicknesses yield a decrease in surface contrasts and directional effects) which is evidenced by

Table 3. Results of *Roujean et al.* [1992] model inversion on POLDER observations

Julian Day	λ nm	k_0	k_1	k_2	$\bar{\rho}$	δ_{obs}	R^2	N	r^2	$\sigma_1^2/\overline{f_1}$	$\sigma_2^2/\overline{f_2}$	det(M) x 10^5
						Shrub Fallow						
237	443	7.76	2.48	-4.81	6.24	0.53	0.71	30	0.49	-0.36	-11.02	3.88
237	570	17.44	6.63	-6.98	13.35	1.46	0.81	30	0.49	-0.36	-11.02	3.88
237	670	24.76	9.55	-9.87	17.88	2.04	0.85	30	0.49	-0.36	-11.02	3.88
237	864	37.32	9.78	5.89	35.24	2.96	0.64	30	0.49	-0.36	-11.02	3.88
247	443	6.75	2.34	-8.94	4.70	0.38	0.76	27	0.72	-0.30	6.11	4.15
247	570	13.19	4.16	-9.31	9 59	0.86	0.73	27	0.72	-0.30	6.11	4.15
247	670	17.63	6.41	-21.95	12.02	1.22	0.60	27	0.72	-0.30	6.11	4.15
247	864	32.55	3.66	27.02	29.66	2.76	0.62	27	0.72	-0.30	6.11	4.15
257	443	6.61	0.47	0.18	6.25	0.24	0.24	21	0.74	-0.28	4.46	2.92
257	570	13.09	2.29	4.14	11.34	0.80	0.77	21	0.74	-0.28	4.46	2.92
257	670	18.28	6.56	-16.73	12.95	0.98	0.84	21	0.74	-0.28	4.46	2.92
257	864	31.63	-1.82	67.89	33.78	3.71	0.64	21	0.74	-0.28	4.46	2.92
261	443	6.84	1.84	-8.80	4.96	0.45	0.40	28	0.74	-0.32	3.24	6.73
261	570	11.34	2.22	-4.24	9.19	0.67	0.53	28	0.74	-0.32	3.24	6.73
261	670	13.18	2.85	-10.15	10.34	0.77	0.38	28	0.74	-0.32	3.24	6.73
261	864	28.57	-1.78	43.80	30.98	2.62	0.57	28	0.74	-0.32	3.24	6.73
278	443	8.30	1.41	-8.41	6.81	0.65	0.30	30	0.50	-0.36	2.43	15.88
278	570	12.89	2.51	-14.67	10.25	0.86	0.54	30	0.50	-0.36	2.43	15.88
278	670	13.68	1.56	-10.33	12 02	0.71	0.35	30	0.50	-0.36	2.43	15.88
278	864	35.38	4.48	-8.89	31.05	2.18	0.31	30	0.50	-0.36	2.43	15.88
						Millet Crop						
237	443	8.93	1.48	-0.44	8.00	0.56	0.31	30	0.35	-0.34	-8.62	4.29
237	570	20.45	3.77	7.65	18.05	1.24	0.68	30	0.35	-0.34	-8.62	4.29
237	670	31.84	6.88	7.31	27.48	2.05	0.68	30	0.35	-0.34	-8.62	4.29
237	864	43.89	5.70	33.13	40.16	2.40	0.88	30	0.35	-0.34	-8.62	4.29
247	443	5.96	-0.13	7.89	6.27	0.85	0.22	27	0.57	-0.36	2.18	11.22
247	570	13.96	1.36	8.48	13.02	1.62	0.26	27	0.57	-0.36	2.18	11.22
247	670	21.28	3.20	4.40	18 67	2.60	0.20	27	0.57	-0.36	2.18	11.22
247	864	33.15	1.09	39.25	33.19	3.43	0.49	27	0.57	-0.36	2.18	11.22
257	443	6.51	-0.88	8 09	7 31	0 43	0.37	22	0.64	-0.30	3.45	4.69
257	570	15.12	1.71	9 82	13 92	0.96	0.80	22	0.64	-0.30	3.45	4.69
257	670	22.49	4.48	0.34	18.99	1.39	0.63	22	0.64	-0.30	3 45	4.69
257	864	37.80	2.94	45.03	36.14	3.34	0.72	22	0.64	-0.30	3.45	4.69
261	443	6.83	1.02	-4.98	5.76	0.52	0.12	26	0.56	-0.26	7.94	4.87
261	570	12.91	1.59	0.51	11.29	0.82	0.30	26	0.56	-0.26	7.94	4.87
261	670	16.19	0.99	3.17	15.20	1.04	0.13	26	0.56	-0.26	7.94	4.87
261	864	29.66	-1.56	51.65	31.51	2.62	0.45	26	0.56	-0.26	7.94	4.87
278	443	9.14	1.76	-9.50	7.26	0.75	0.48	30	0.31	-0.34	2.85	19.10
278	570	15.18	3.19	-17.81	11.77	1.11	0.72	30	0.31	-0.34	2.85	19.10
278	670	18.53	2.88	-16.31	15.44	1.29	0.44	30	0.31	-0.34	2.85	19.10
278	864	36.15	4.55	-5.88	31.63	1.83	0.58	30	0.31	-0.34	2.85	19.10
						Degraded Shrubland						
237	443	5.39	-0.76	-0.31	6.19	0.52	0.10	13	0.16	-0.21	-0.37	0.72
237	570	14.29	0.16	10.82	13.72	0.70	0.04	13	0.16	-0.21	-0.37	0.72
237	670	26.26	3.39	44.26	21.12	1.77	0.19	13	0.16	-0.21	-0.37	0.72
237	864	31.08	-2.92	6.17	33.86	1.27	0.30	13	0.16	-0.21	-0.37	0.72
247	443	6.72	1.67	-5.50	5.33	0.38	0.30	21	0.82	-0 60	0.62	7.06
247	570	15.19	3.93	-9.94	12.25	0.87	0.44	21	0.82	-0.60	0.62	7.06
247	670	22.50	5.23	-10.75	18.87	1.43	0.37	21	0.82	-0.60	0.62	7.06
247	864	36.04	6.71	-3.04	32.59	2.13	0.66	21	0.82	-0.60	0.62	7.06
257	443	5.60	-1.79	6.92	7.27	0.70	0.16	13	0.81	-0.47	1.55	14.49
257	570	15.51	2.43	-1.56	13.64	0.81	0.89	13	0.81	-0.47	1.55	14.49
257	670	22.19	3.64	1.91	19.61	1.50	0.95	13	0.81	-0.47	1.55	14.49
257	864	38.08	4.66	6.78	34.99	2.28	0.94	13	0.81	-0.47	1.55	14.49
261	443	5.72	-0.39	1.95	6.13	0.22	0.09	11	0.74	-0.31	0.90	4.59
261	570	11.80	-0.16	2.09	12.06	0.36	0.08	11	0.74	-0.31	0.90	4.59
261	670	15.76	-1.11	6.93	17.01	0.50	0.27	11	0.74	-0.31	0.90	4.59
261	864	35.23	3.43	16.74	33.95	1.90	0.89	11	0.74	-0.31	0.90	4.59
278	443	4.57	-1.82	14.77	6.80	0.93	0.27	19	0.39	-0.25	2.71	7.07
278	570	7.93	-1.92	14.07	10.26	1.01	0.22	19	0 39	-0.25	2.71	7.07
278	670	10.58	-3.27	24.77	14.56	1.38	0.36	19	0.39	-0.25	2.71	7.07
278	864	19.61	-4.91	52.02	25.79	2.07	0.60	19	0.39	-0.25	2.71	7.07

Parameter $\bar{\rho}$ is the mean and δ_{obs} is the standard deviation of the measurements. R^2 is the coefficient of determination between observed and modeled reflectances. N is the number of observations; r^2 is the coefficient of determination between the directional kernels f_1 and f_2; $\sigma_1^2/\overline{f_1}$ and $\sigma_2^2/\overline{f_2}$ are the relative variances; det(M) is the determinant of the M matrix used for the retrieval of k_0, k_1, and k_2 (see text).

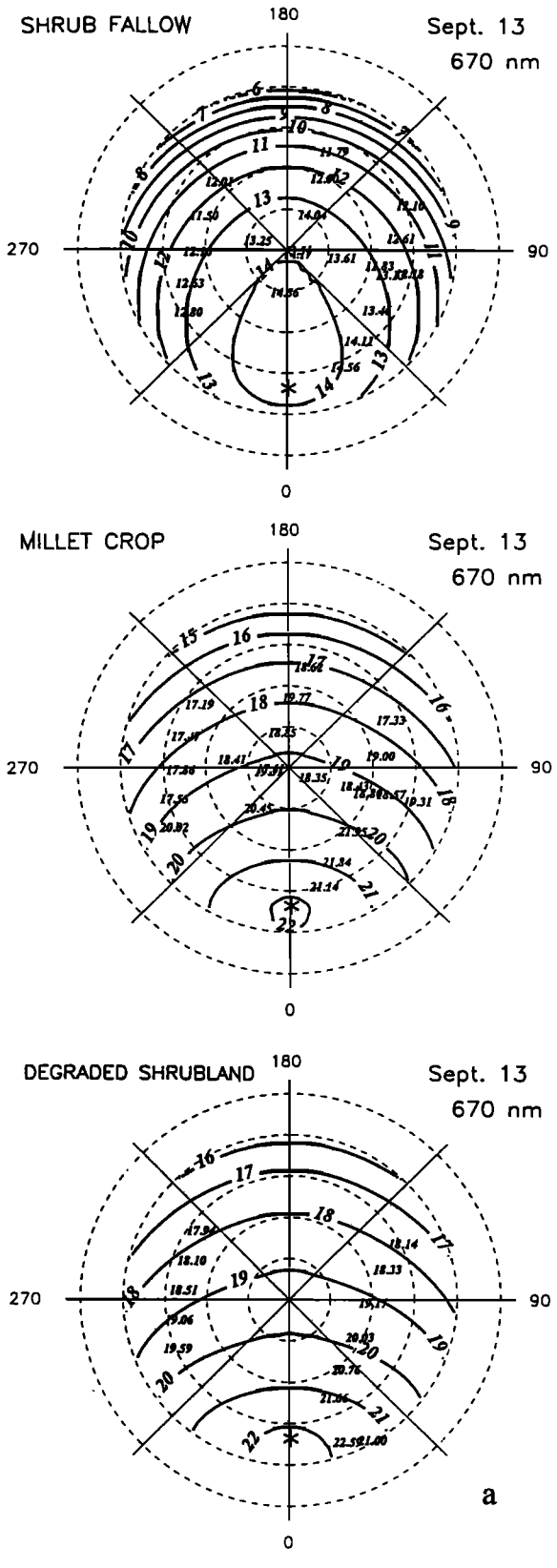

Figure 6a. Surface bidirectional reflectance, derived from POLDER measurements, on September 13 for the three selected sites. The measurement points, which have been acquired with a mean solar zenith angle of 52.5°, are displayed and indicate the flight axis. The lines are for the model estimates, for a solar angle of 52.5°, after inversion on the measurements.

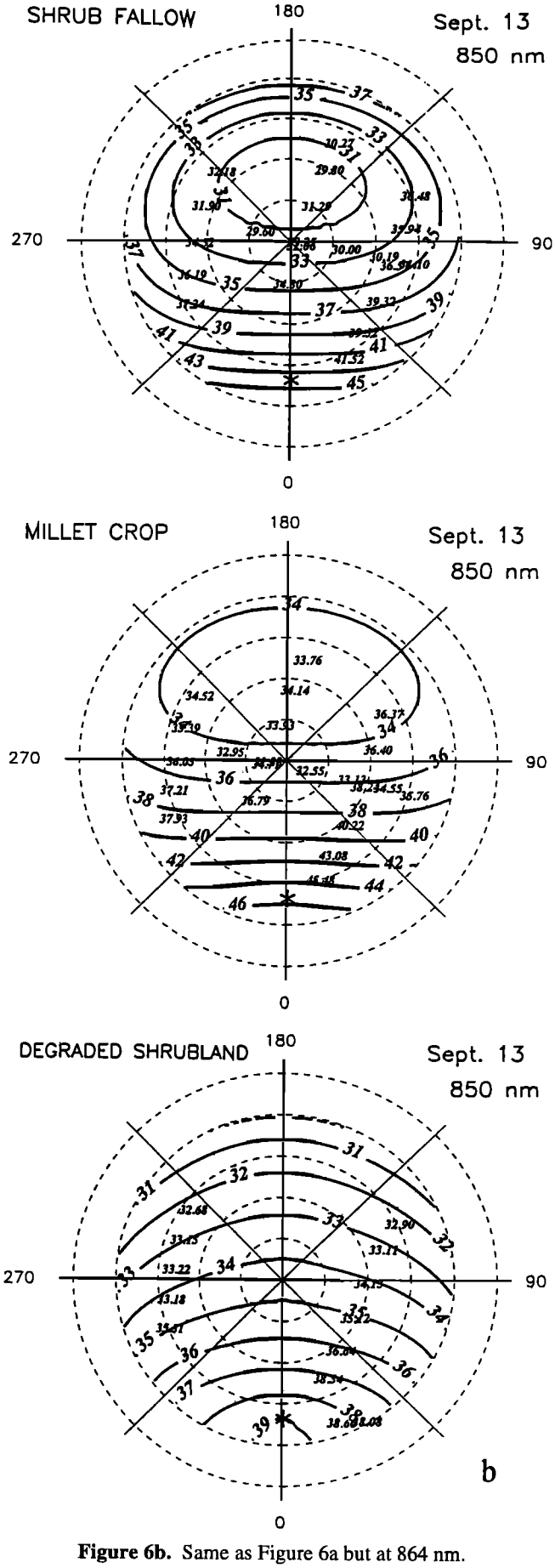

Figure 6b. Same as Figure 6a but at 864 nm.

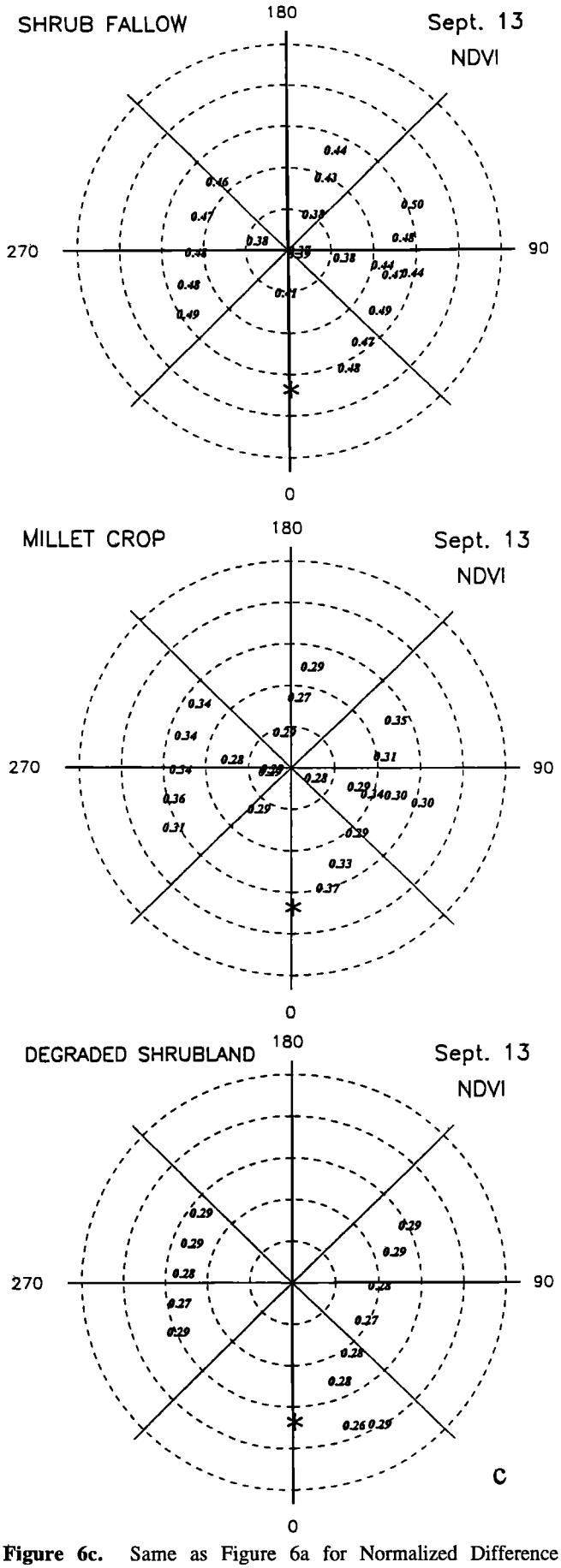

Figure 6c. Same as Figure 6a for Normalized Difference Vegetation Index (NDVI).

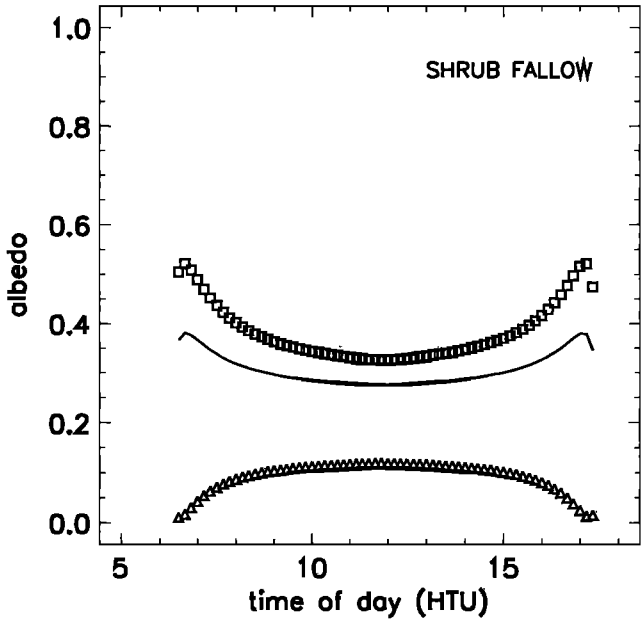

Figure 7. Diurnal variation of the shrub fallow albedo on September 13 at 670 nm (triangles), 864 nm (squares), and broadband (line). The albedo is derived from the model bidirectional reflectance, after inversion on POLDER measurements.

the poor correlation between observed and modeled reflectances for this date (see Table 3). Since the protrusion parameter is estimated from the variations of background shadows, it is better determined on clear sky conditions. Similarly, the estimate would be more accurate using measurements acquired with different Sun angles. The values of z_0 obtained with (20) are

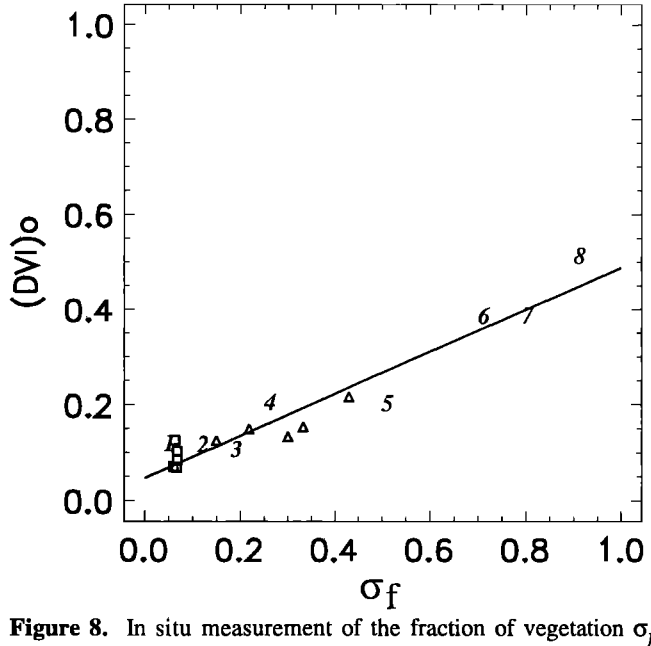

Figure 8. In situ measurement of the fraction of vegetation σ_f and the vegetation index $(DVI)_0$ as measured by POLDER for the shrub fallow (triangles) and the millet crop (squares). The figure also reports some results from *Kimes* [1983] and *Kimes et al.* [1985, 1986]. 1, Annual grass; 2, hard wheat; 3, steppe; 4, corn; 5, orchard grass; 6, irrigated wheat; 7, deciduous forest; 8, soybean [see *Roujean et al.*, 1992, Table 1, for more].

Table 4. Seasonal Variation of the Albedo, the Protrusion Parameter $(k_1/k_0)_{670}$, and the Aerodynamic Roughness z_0 Derived from POLDER Observations

	Aug. 24	Sept. 3	Sept. 13	Sept. 17	Oct. 4
			Shrub Fallow		
	10.2	5.80	7.30	7.90	10.0
Diffuse albedo 864 nm (%)	24.8	31.5	43.3	37.2	27.9
Broadband albedo (%)	21.2	24.4	33.6	29.4	23.4
Protrusion parameter, 670 nm	0.38	0.36	0.36	0.22	0.11
z_0 (cm)	28.5	27.0	27.0	16.5	8.30
			Millet Crop		
Diffuse albedo, 670 nm (%)	23.5	17.6	16.6	15.3	12.2
Diffuse albedo, 864 nm (%)	41.0	37.4	40.0	39.1	29.1
Broadband albedo (%)	37.8	33.0	34.6	33.5	25.0
Protrusion parameter, 670 nm	0.22	0.15	0.20	0.06	0.16
z_0 (cm)				6.50	

lower than 30 cm for shrub fallow (Table 4), which complies with the order of magnitude of expected values for such canopies. This value becomes 6.5 cm for millet, which is unsually small since the sample crop was a very sparse canopy. However, additional work is needed for the validation of this approach, for instance in comparing estimates made over a larger spatial scale with values retrieved in adjusting measured and modeled energy fluxes.

5. Summary and Discussion

During the HAPEX-Sahel experiment, the airborne POLDER instrument acquired reflectance measurements over various typical surfaces of the Sahel environment. The unique design of this radiometer allows the measurement of the surface directional signature for viewing angles up to 60°. The reflectance was found to be much larger in the backscattering direction than in the forward scattering direction. The model of *Roujean et al.* [1992] complies with the requirements given by *Dickinson et al.* [1990], and is well adapted to the case of heterogeneous surfaces, owing to its linear formulation. After an inversion of the three model parameters through a regression procedure, the modeled reflectances comply with the measurements in the range of accessible viewing angles. It allows extrapolation of the measurements to the full hemisphere and thus generation of an accurate estimate of the surface albedo. This model was selected to derive global albedo products from spaceborne POLDER.

The reflectance model was also used to generate data in certain Sun/view geometry for a retrieval of surface parameters of interest for GCMs. Because typical Sahel landscapes show low vegetation coverage and bright soil, a minimization of the soil contribution to the measurement is sought. We proposed relationships which relate the model parameters, inverted from the measurements, and some surface or vegetation parameters of interest (vegetation coverage, vegetation PAR absorption, LAI, surface roughness). Surface measurements of these parameters have been done in the context of the HAPEX-Sahel experiment, which allowed either to derive the relationships or to validate those which could be inferred physically. The accuracy on the retrieved parameters is in agreement with the objectives of the study, which are to propose methods to be further used for a regional mapping of surface properties. The relationships which

Table 5. In Situ Measurements of Some Optical Variable Characteristics of Selected Vegetation Sites, September 25

	Shrub Fallow		*Millet Crop*	
	PAR	Near Infrared	PAR	Near Infrared
	0.4-0.7 μm	0.7-1.1 μm	0.4-0.7 μm	0.7-1.1 μm
r t	0.12 0.04	0.43 0.35	0.13 0.03	0.45 0.40
$\omega=r+t$	0.16	0.78	0.17	0.85
g	- 0.22	-0.04	- 0.23	-0.03
b	0.94		0.93	

PAR, photosynthetically active radiation.

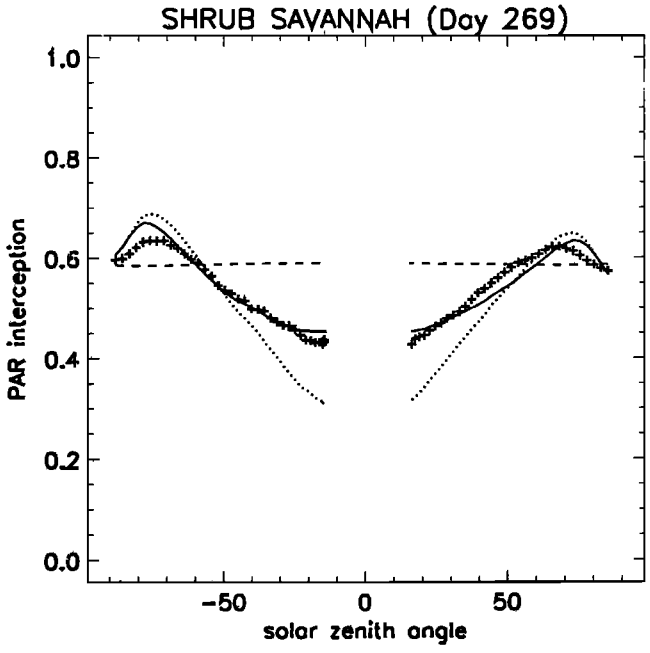

Figure 9. Hourly photosynthetically active radiation (PAR) interception on the shrub fallow on September 25, measured (pluses) and simulated for a planophile canopy (dashed), a spherical canopy (line) and an erectophile canopy (dotted).

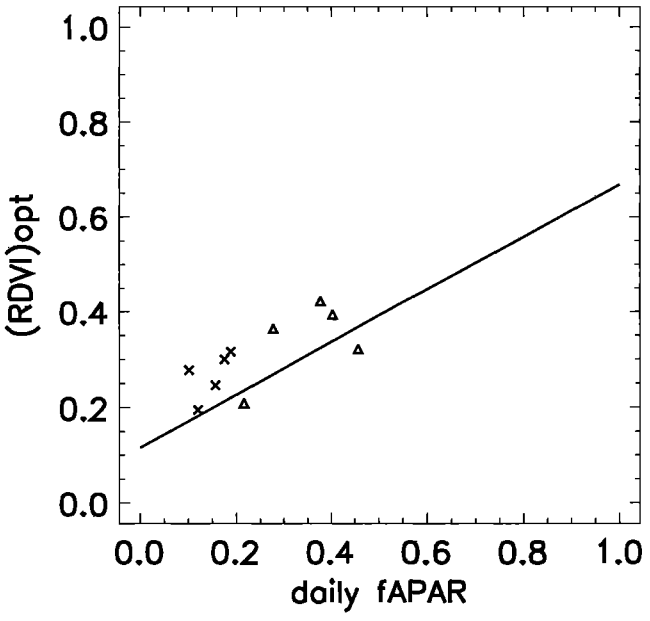

Figure 11. In situ measurement of daily $\overline{f_{APAR}}$ as a function of vegetation index $(RDVI)_{opt}$ as measured by POLDER for the shrub fallow (triangles) and millet crop (crosses). The line is from a theoretical analysis [e.g., *Roujean and Bréon*, 1995].

are proposed in this paper should now be tested over other landscapes in order to investigate their robustness and degree of generality.

The study presented in this paper makes use of directional signature measurements to derive surface parameters which could not be inferred accurately from a single directional measurement. In the context of current spaceborne Earth monitoring, the capacity for directional signature measurements are very limited. AVHRR provides only one measurement per orbit, and multiorbit measurements of a given surface target are limited to a small range of azimuth angles. The ATSR-2 onboard the ERS-2 platform provides two measurements per orbit, which is also insufficient. On the other hand, the POLDER instrument onboard ADEOS will provide up to 14 directional measurements of a given surface target per orbit and a near complete sampling of the BRDF within a few days of observation. Assuming that the BRDF can be derived from satellite observations, the strategy for surface parameter retrieval is not yet clear. A full inversion of a physical BRDF model may be preferred since it can generate directly the parameters describing the canopy. However, these models assume a homogeneous target within the instrument field of view, which may not be appropriate for spaceborne remote sensing. Another option is to extrapolate the directional measurements, using a physical or empirical model, to an optimal geometry for which the surface parameters can be derived. In some cases this approach favors large viewing angles because it minimizes the relative contribution of the soil and vegetation underlayer. On the other hand, such viewing geometry increases the atmospheric effect on the measurement and the extrapolation to large viewing angles may be in error. Thus one may favor a normalization of the measurements to nadir viewing. It is expected that other measurements, such as using POLDER data over various landscapes, will bring new insights to this question.

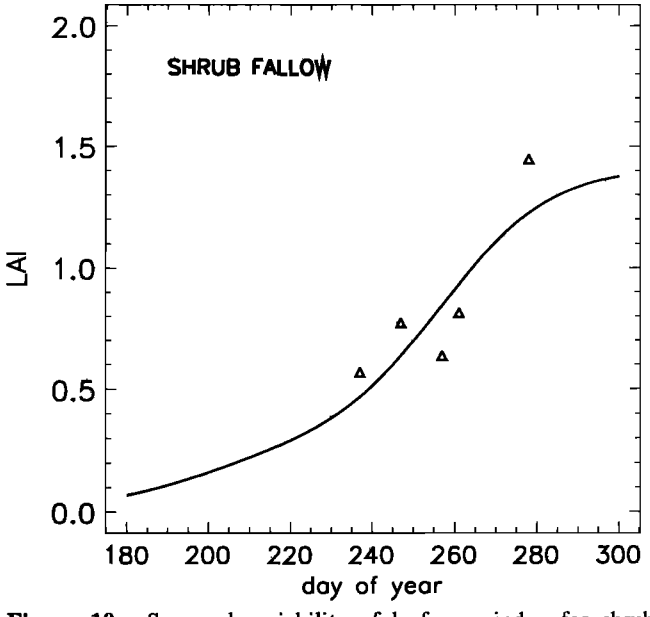

Figure 10. Seasonal variability of leaf area index for shrub fallow on Central West site as measured (line) and derived from POLDER measurements of $(DVI)_0$ (triangles).

Acknowledgments. This work was performed in the framework of the Hydrology and Atmospheric Pilot Experiment and was supported by the European Economic Community under contract EV5V-CT91-0033 and by the Programme National de Télédétection Spatiale. The authors are very indebted to Frédéric Lemire from LOA who performed the major part of the POLDER image processing. We also thank Météo France and LOA for technical assistance. Two of us (FMB and JLR) received financial support from CNES as postdoctoral fellows.

References

Allen, S. J, J. S. Wallace, J. H. C. Gash, and M. V. K. Sivakumar, Measurements of albedo variation over natural vegetation in the Sahel, *Int. J. Climat., 14*, 625-636, 1994.

Asrar, G., M. Fichs, E. T. Kanemasu, and J. L. Hatfield, Estimating absorbed photosynthetically active radiation and leaf area index from spectral reflectance in wheat, *Agron. J., 76*, 300-306, 1984.

Bégué, A., Modeling hemispherical and directional radiative fluxes in regular-clumped canopies, *Remote Sens. Environ., 40*(3), 219-230, 1992.

Bégué, A., J. L. Roujean, N. P. Hanan, S. D. Prince, M. Thawley, A. Huete, and D. Tanré, Shortwave radiation budget of Sahelian vegetation during HAPEX-Sahel, 1, Techniques of measurement and results, *Agric. For. Meteorol., 79*, 79-96, 1996a.

Bégué, A., S. D. Prince, N. P. Hanan, and J. L. Roujean, Shortwave radiation budget of Sahelian vegetation during HAPEX-Sahel, 2, Radiative transfer models, *Agric. For. Meteorol., 79*, 97-112, 1996b.

Charney, J., W. J. Quirk, S. M. Chow, and J. Kornfield, A comparative study of the effects of albedo change on drought in semi-arid regions, *J. Atmos. Sci., 34*, 1366-1385, 1977.

Chen, J. M., and T. A. Black, Measuring leaf area index of plant canopies with branch architecture, *Agric. For. Meteorol., 57*, 1-12, 1991.

Deardorff, J. W., Efficient prediction of ground surface temperature and moisture with inclusion of a layer of vegetation, *J. Geophys. Res., 20*, 1889-1903, 1978.

Deschamps, P. Y., F. M. Bréon, M. Leroy, A. Podaire, A. Bricaud, J. C. Buriez, and G. Sèze, The POLDER mission: Instrument characteristics and scientific objectives, *IEEE Trans. Geosci. Remote Sens., GE-32*, 598-615, 1994.

Deuzé, J. L., F. M. Bréon, P. Y. Deschamps, C. Devaux, M. Herman, A. Podaire, and J. L. Roujean, Analysis of the POLDER (POLarization and Directionality of Earth's Reflectances) airborne instrument observations over land surfaces, *Remote Sens. Environ., 45*, 137-154, 1993.

Devaux, C., M. Herman, R. Santer, and D. Tanré, On the complementarity of solar transmission and aureole measurements to derive the aerosol size distribution. Applications to desert aerosol characteristics retrievals, in *IRS'88 Current Problems in Atmospheric Radiation*, edited by J. Lenoble and J.F. Geleyn, pp. 557-560, A. Deepak, Hampton, Va., 1989.

Dickinson, R. E., Land surface processes and climate-surface albedos and energy balance, *Adv. Geophys., 25*, 305-353, 1983.

Dickinson, R. E., A. Henderson-Sellers, P. J. Kennedy, and M. F. Wilson, Biosphere-atmosphere transfer scheme (BATS) for the NCAR community climate model, *NCAR Tech. Note/TN-275+STR*, 69 pp., Nat. Cent. Atmos. Res., Boulder, Colo., 1986.

Dickinson, R. E., B. Pinty, and M. M. Verstraete, Relating surface albedos in GCM to remotely sensed data, *Agric. For. Meteorol., 52*, 109-131, 1990.

Fraser, R. S., and Y. J. Kaufman, The relative importance of scattering and absorption in remote sensing, *IEEE Trans. Geosci. Remote Sens., GE-23*, 699-708, 1985.

Fung, I. Y., C. J. Tucker, and K. C. Prentice, Application of advanced very high resolution radiometer vegetation index to study atmosphere-biosphere exchange of CO_2, *J. Geophys. Res., 92*, 2999-3015, 1987.

Goutorbe, J. P., et al., HAPEX-Sahel: A large-scale study of land-atmosphere interactions in the semi-arid tropics, *Ann. Geophys., 12*, 53-64, 1994.

Goward, S. N., and K. F. Huemmrich, Vegetation canopy PAR absorptance and the Normalized Difference Vegetation Index: An assessment using the SAIL model, *Remote Sens. Environ., 39*, 119-140, 1992.

Hapke, B., Bidirectional reflectance spectroscopy, 4, The extinction coefficient and the opposition effect, *Icarus, 67*, 264-280, 1986.

Henderson-Sellers, A., Intercomparison of land-surface parameterizations launched, *Eos Trans. AGU, 73*, 195-196, 1992.

Huete, A. R., A Soil-Adjusted Vegetation Index (SAVI), *Remote Sens. Environ., 25*, 295-309, 1988.

Jupp, D. L., and A. H. Strahler, A hot-spot model for leaf canopies, *Remote Sens. Environ., 38*, 193-210, 1991.

Kimes, D. S., Dynamics of directional reflectance factor distribution for vegetation canopies, *Appl. Opt., 22*, 1364-1372, 1983.

Kimes, D. S., and P. J. Sellers, Inferring hemispherical reflectance of the earth's surface for global energy budgets from remotely sensed nadir of directional radiance values, *Remote Sens. Environ., 18*, 205-223, 1985.

Kimes, D. S., W. W. Newcomb, C. J. Tucker, I. S. Zonneveld, W. Van Wijngaarden, J. de Leeuw, and G. F. Epema, Directional reflectance factor distributions for cover types of Northern Africa, *Remote Sens. Environ., 18*, 1-19, 1985.

Kimes, D. S., W. W. Newcomb, R. F. Nelson, and J. B. Schutt, Directional reflectance distributions of a hardwood and a pine forest canopy, *IEEE Trans. Geosci. Remote Sens., GE-24*, 281-293, 1986.

Kimes, D. S., P. J. Sellers, and D. J. Diner, Extraction of spectral hemispherical reflectance (albedo) of surfaces from nadir and directional reflectance data, *Int. J. Remote Sens., 8*, 1727-1746, 1987.

Kumar, M., and J. L. Monteith, Remote sensing of crop growth, in *Plants and the Daylight Spectrum*, edited by H. Smith, pp. 133-144, Academic, San Diego, Calif., 1981.

Kuusk, A., The hot spot effect of a uniform vegetative cover, in *Earth Research Space, vol. 4*, pp. 90-99, 1983. (Russ./Engl. transl. *Sov. J. Remote Sens., 3*(4), 645-658, 1985).

Lee, T., and Y. J. Kaufman, The effect of surface non-Lambertianity on remote sensing of ground reflectance and vegetation index, *IEEE Trans. Geosci. Remote Sens., GE-24*, 699-708, 1986.

Lenoble, J., *Atmospheric Radiative Transfer*, 532 pp., A. Deepak, Hampton, Va, 1993.

Leroy, M., and J. L. Roujean, Sun and view angle corrections on reflectances derived from NOAA/AVHRR data, *IEEE Trans. Geosci. Remote Sens., GE-32*, 684-697, 1994.

Lettau, H., Note on aerodynamic roughness-parameter estimation on the basis of roughness-element description, *J. Appl. Meteorol., 8*, 828-832, 1969.

Mintz, Y., The sensitivity of numerically simulated climates to land-surface conditions, in *The Global Climate*, edited by J. Houghton, pp. 79-105, Cambridge Univ. Press, New York, 1984.

Myneni, R. B., and D. L. Williams, On the relationship between FAPAR and NDVI, *Remote Sens. Environ., 49*, 200-211, 1994.

Nilson, T., A theoretical analysis of the frequency of gaps in plant stands, *Agric. Meteorol., 8*, 25-38, 1971.

Noilhan, J., and S. Planton, A simple parameterization of land surface processes for meteorological models, *Mon. Weather Rev., 117*, 536-549, 1989.

Otterman, J., and C. J. Tucker, Satellite measurements of surface albedo and temperatures in semi-desert, *J. Clim. Appl. Meteorol., 24*, 228-235, 1985.

Prince, S. D., A model of regional primary production for use with coarse resolution satellite data, *Int. J. Remote Sens., 12*(6), 1313-1330, 1991.

Ross, J. K., *The Radiation Regime and Architecture of Plant Stands*, 391 pp., Dr W. Junk, Norwell, Mass., 1981.

Roujean, J. L., and F. M. Bréon, Estimating PAR absorbed by vegetation from bidirectional reflectance measurements, *Remote Sens. Environ., 51*, 375-384, 1995.

Roujean, J. L., M. Leroy, and P. Y. Deschamps, A bidirectional reflectance model of the Earth's surface for the correction of remote sensing data, *J. Geophys. Res., 97*, 20,455-20,468, 1992.

Rowe, C. M., Incorporating landscape heterogeneity in land surface albedo models, *J. Geophys. Res., 98*, 5037-5043, 1993.

Sagan, C., and J. B. Pollack, Anisotropic nonconservative scattering and the clouds of Venus, *J. Geophys. Res., 72* , 469-477, 1967.

Sato N., P. J. Sellers, D. A. Randall, E. K. Schneider, J. Shukla, J. L. Kinter III, Y. T. Hou, and E. Albertazzi, Effects of implementing the simple biosphere model (SiB) in a general circulation model, *J. Atmos. Sci., 46(18)*, 2757-2782, 1989.

Sellers, P. J., Canopy reflectance, photosynthesis and transpiration, *Int. J. Remote Sens., 6*, 1335-1372, 1985.

Sellers, P. J., Canopy reflectance, photosynthesis and transpiration, II, The role of biophysics in the linearity of their interdependence, *Remote Sens. Environ., 21*, 143-183, 1987.

Sellers, P. J., Y. Mintz, Y. C. Sud, and A. Dalcher, A simple biosphere model (SiB) for use within General Circulation Models, *J. Atmos. Sci., 43*(6), 505-531, 1986.

Smith, E. A., H. J. Cooper, W. L. Crosson, and W. Heng-Yi, Estimation of surface heat and moisture fluxes over a prairie grassland, 3, Design of a hybrid physical/remote sensing biosphere model, *J. Geophys. Res., 98*, 4951-4978, 1993.

Tanré, D., M. Herman, P. Y. Deschamps, and A. de Leffe, Atmospheric modeling for space measurements of ground reflectances including bidirectional properties, *Appl. Opt, 18(21)*, 3587-3594, 1979.

Tanré, D., C. Devaux, M. Herman, R. Santer, and J. Y. Gac, Radiative properties of desert aerosols by optical ground-based measurements at solar wavelengths, *J. Geophys. Res., 93*, 14,223-14,231, 1988.

Walthall, C. L., J. M. Norman, J. M. Welles, G. Campbell, and B. L. Blad,

Simple equation to approximate the bidirectional reflectance from vegetative canopies and bare soil surfaces, *Appl. Opt., 24*(3), 383-387, 1985.

Wydick, J. E., P. A. Davies and A. Gruber, Estimation of broadband planetary albedo from operational narrowband satellite measurements, *NOAA Tech. Rep. NESDIS 27*, 32 pp., U.S. Dep. of Comm., Washington, D.C., 1987.

F.-M. Bréon, Commissariat à l'Energie Atomique/Laboratoire de Modélisation du Climat et de l'Environnement, 91191 Gif sur Yvette, France. (e-mail: fmbreon@cea.fr)

J.-L. Deuzé and D. Tanré, Laboratoire d'Optique Atmosphérique, URA CNRS 713, Université des Sciences et Techniques de Lille, 59655 Villeneuve d'Ascq Cedex, France. (e-mail: deuze@loa.univ-lille1.fr; tanre@loa.univ-lille1.fr)

J.-L. Roujean, GAME/CNRM (Météo France/CNRS), 42, avenue Gustave Coriolis, 31057 Toulouse Cedex, France. (e-mail: roujean@meteo.fr)

(Received March 5, 1996; revised December 17, 1996;
accepted January 15, 1997.)